Estimating model parameters for an impact-produced shock-wave simulation: Optimal use of partial data with the extended Kalman filter

Jim Kao [a,*], Dawn Flicker [a], Kayo Ide [b], Michael Ghil [b,1]

[a] *Los Alamos National Laboratory, Applied Physics Division, P.O. Box 1663, MS T086, Los Alamos, NM 87545, United States*
[b] *University of California at Los Angeles, United States*

Abstract

This paper builds upon our recent data assimilation work with the extended Kalman filter (EKF) method [J. Kao, D. Flicker, R. Henninger, S. Frey, M. Ghil, K. Ide, Data assimilation with an extended Kalman filter for an impact-produced shock-wave study, J. Comp. Phys. 196 (2004) 705–723.]. The purpose is to test the capability of EKF in optimizing a model's physical parameters. The problem is to simulate the evolution of a shock produced through a high-speed flyer plate. In the earlier work, we have showed that the EKF allows one to estimate the evolving state of the shock wave from a single pressure measurement, assuming that all model parameters are known. In the present paper, we show that imperfectly known model parameters can also be estimated accordingly, along with the evolving model state, from the same single measurement.

The model parameter optimization using the EKF can be achieved through a simple modification of the original EKF formalism by including the model parameters into an augmented state variable vector. While the regular state variables are governed by both deterministic and stochastic forcing mechanisms, the parameters are only subject to the latter. The optimally estimated model parameters are thus obtained through a unified assimilation operation. We show that improving the accuracy of the model parameters also improves the state estimate.

The time variation of the optimized model parameters results from blending the data and the corresponding values generated from the model and lies within a small range, of less than 2%, from the parameter values of the original model. The solution computed with the optimized parameters performs considerably better and has a smaller total variance than its counterpart using the original time-constant parameters. These results indicate that the model parameters play a dominant role in the performance of the shock-wave hydrodynamic code at hand.
© 2005 Elsevier Inc. All rights reserved.

1. Introduction

Data assimilation estimates the evolving state of a dynamic system by merging sparse data into a numerical model of the system [3,11]. The extended Kalman filter (EKF) method of data assimilation [10,11,15,20] was

* Corresponding author. Tel.: +1 505 667 9226; fax: +1 505 667 4420.
  E-mail address: kao@lanl.gov (J. Kao).
[1] Also affiliated with Ecole Normale Supérieure, Paris, France.

designed to optimize predictions of, as well as reduce uncertainties in, the modeled state variables, provided that the errors in the observations and model performance can be estimated. The EKF algorithm tracks the nonlinear state evolution and its associated error-covariance matrix in time. It provides a consistent first-order approximation to the optimal estimate of the state and of the time-dependent model uncertainties, both when data are available and when they are not.

We have recently applied the EKF method of data assimilation [20] to a one-dimensional (1-D) hydrodynamic shock-wave code [4] with a limited amount of pressure data measured at a single location. The underlying physical problem stems from a flyer plate experiment [16]. Our results [20] successfully demonstrated that: (1) EKF propagates information through the model's governing equations from observed to unobserved variables as well as locations; (2) EKF should not be considered a curve fitting procedure; carefully assessing both the model and observation errors is crucial in obtaining meaningful results with this method; and (3) a single scalar observation can noticeably reduce the error in estimating the state of the 1-D system with its total number of over 200 discrete variables.

Our previous work also pointed out that, when the model evolution without data assimilation systematically deviates from the experimental data, the model's assimilated fields can even quickly lose track of the data and drift into the model's original solution. This model property explains the repetitively restoring, zig–zag features of the assimilated evolution in the release period of the shock wave, where the model systematically predicts a sharper fall-off in pressure than the data; see further discussion in Section 4.1 of the present paper. The most likely physical reasons for any substantial discrepancies between measurements and model evolution are the following: (1) inadequate model physics; (2) incorrect physical parameters used in the model; and (3) systematic errors in the measurements. The current paper attempts to shed some lights on the second reason, while fully recognizing that it is potentially related to the first.

The determination of a model's physical parameters has always been an important task in modeling studies. Ideally, information from experimental data, based on a respectable number of realizations for statistical confidence, is needed. The model is then "closed" with a set of constant parameters through certain fitting procedures. However, often times, model users do not have at their disposal a judiciously determined set of parameters and, therefore, use trial-and-error to "tune" their model parameters for the specific physical situation of interest. In the modern system-identification theory [21], the process of parameter estimation yields model parameters from existing observations and prior dynamical knowledge as represented by the model itself. The present study follows this latter route.

Any dynamic system in science and technology is potentially influenced by stochastic forcing mechanisms. While the state variables in the modeled system are allowed to be subject to uncertainties, the model's physical parameters are conventionally assumed to be constant in time. This is equivalent to letting the state variables absorb the uncertainties present in the parameters. However, as the system undergoes physically distinct stages, the above-mentioned shifting of the uncertainties may fail to produce a reasonable evolution of model states.

Several methodologies are available, as summarized in [10,12,24], for parameter estimation purposes. EKF is the only method that accounts for both model and measurements errors, as well as allowing sequential processing of the data as they become available. A natural question then arises: since EKF would result in model parameters that vary in time as data come in, what would the physical interpretation of these time-varying parameters be? The answer to this question depends on whether the range of the variation is within the accepted uncertainties validated by laboratory experiments. This issue is especially pertinent for shock-wave studies since shocks involve two extremely different physical regimes, in both space and time: the regime in front of the shock and the one behind it.

Data assimilation, in general, serves two purposes: better prediction and better understanding of the fundamental physics. If the underlying dynamics of a system is not fully known, data assimilation may help unravel a model's built-in deficiencies. Our investigation is based on the simple flyer plate experiment [25] in a 1-D configuration, as described in our previous work [20].

The present paper is organized as follows. In Section 2, we give a brief review of the EKF method and show how the parameter estimation is achieved with a unified EKF framework. Section 3 reviews the MESA-1D code and the flyer plate experiments. The results of applying EKF to both state and parameter estimation appear in Section 4. Concluding remarks follow in Section 5.

2. The extended Kalman filter (EKF)

2.1. A review of EKF

A detailed formulation of the EKF can be found in [10,11,15,17,23]. Its actual implementation in our flyer-plate shock-wave simulations is described in [20]. Only a brief review of the EKF method is given here, using Fig. 1 and Table 1, in continuous time.

The EKF method estimates the true evolution of a physical system, from the system's deterministic dynamics and its observations, through a simple probabilistic analysis. The true evolution is governed by a nonlinear stochastic differential equation, Eq. (2.1) in Fig. 1, where the stochastic forcing (or system noise) $d\boldsymbol{\eta}$ represents model errors, in particular due to unknown subgrid-scale processes. This forcing is modeled by a Wiener process with zero mean and a covariance matrix $\mathbf{Q}$ defined by Eq. (2.2).

The EKF has two stages: the prediction and update stage. The prediction stage is represented by Eqs. (2.5) and (2.6), which govern the time rates of change of the state vector $\mathbf{x}^p$ and the covariance matrix $\mathbf{P}^p$, respectively. The latter is defined by Eq. (2.4) and its trace $\mathrm{tr}\mathbf{P}^p$ is a global measure of prediction error. The right-hand-side $\mathbf{m}(\mathbf{x}^p, t)$ of Eq. (2.5) represents the deterministic processes in the system. The Jacobian matrix $\mathbf{M}$ in Eq. (2.7) is the linearized transition matrix. The observations $\mathbf{y}^o$ and associated errors ε are defined by Eq. (2.8), with their error covariance matrix $\mathbf{R}$ defined by Eq. (2.9). With these observations, the update stage proceeds. The EKF updates $\mathbf{x}^p$ to $\mathbf{x}^a$ and $\mathbf{P}^p$ to $\mathbf{P}^a$ by Eqs. (2.12) and (2.13), respectively. Within these two equations, $\mathbf{d}^{op}$ represents the difference between the observation and prediction, expressed by Eq. (2.10), $\mathbf{K}$ is the Kalman gain matrix expressed by Eq. (2.14), and $\mathbf{H}$ is the Jacobian of the observation function $\mathbf{h}$ defined by Eq. (2.11) as the linearized observation matrix. Finally, the Kalman gain matrix $\mathbf{K}$ is obtained by minimizing the trace of $\mathbf{P}^a$.
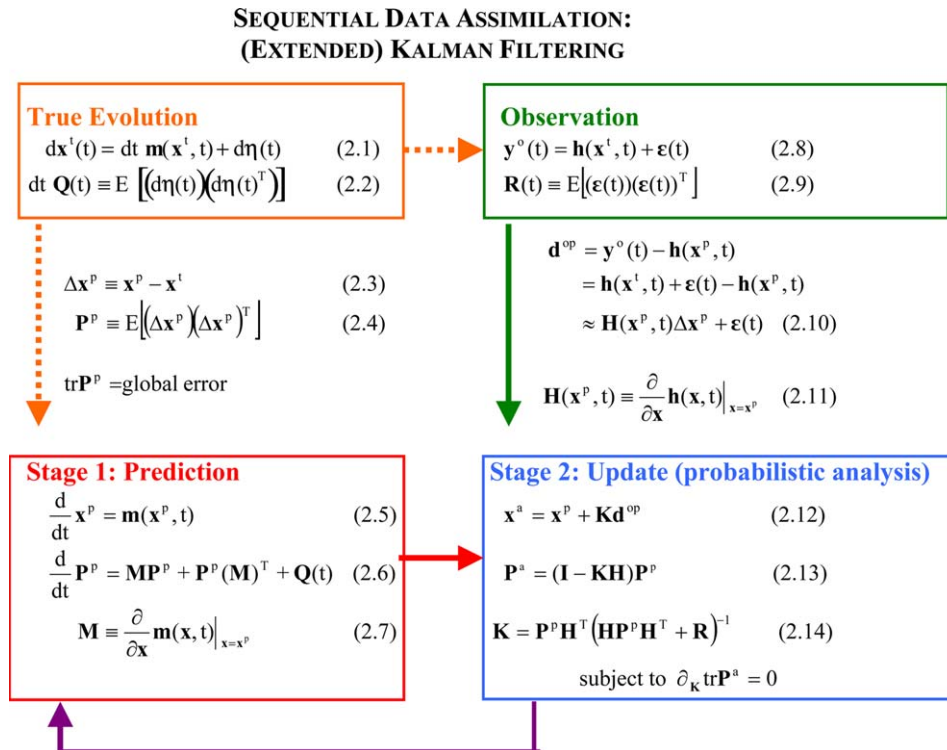

SEQUENTIAL DATA ASSIMILATION: (EXTENDED) KALMAN FILTERING

True Evolution

$$d\mathbf{x}^t(t) = dt\, \mathbf{m}(\mathbf{x}^t, t) + d\boldsymbol{\eta}(t) \quad (2.1)$$

$$dt\, \mathbf{Q}(t) \equiv E\left[(d\boldsymbol{\eta}(t))(d\boldsymbol{\eta}(t)^{\mathrm{T}})\right] \quad (2.2)$$

$$\Delta\mathbf{x}^p \equiv \mathbf{x}^p - \mathbf{x}^t \quad (2.3)$$

$$\mathbf{P}^p \equiv E\left[(\Delta\mathbf{x}^p)(\Delta\mathbf{x}^p)^{\mathrm{T}}\right] \quad (2.4)$$

$$\mathrm{tr}\mathbf{P}^p = \text{global error}$$

Observation

$$\mathbf{y}^o(t) = \mathbf{h}(\mathbf{x}^t, t) + \boldsymbol{\varepsilon}(t) \quad (2.8)$$

$$\mathbf{R}(t) \equiv E\left[(\boldsymbol{\varepsilon}(t))(\boldsymbol{\varepsilon}(t))^{\mathrm{T}}\right] \quad (2.9)$$

$$\mathbf{d}^{op} = \mathbf{y}^o(t) - \mathbf{h}(\mathbf{x}^p, t)$$
$$= \mathbf{h}(\mathbf{x}^t, t) + \boldsymbol{\varepsilon}(t) - \mathbf{h}(\mathbf{x}^p, t)$$
$$\approx \mathbf{H}(\mathbf{x}^p, t)\Delta\mathbf{x}^p + \boldsymbol{\varepsilon}(t) \quad (2.10)$$

$$\mathbf{H}(\mathbf{x}^p, t) \equiv \frac{\partial}{\partial\mathbf{x}}\mathbf{h}(\mathbf{x}, t)\Big|_{\mathbf{x}=\mathbf{x}^p} \quad (2.11)$$

Stage 1: Prediction

$$\frac{d}{dt}\mathbf{x}^p = \mathbf{m}(\mathbf{x}^p, t) \quad (2.5)$$

$$\frac{d}{dt}\mathbf{P}^p = \mathbf{M}\mathbf{P}^p + \mathbf{P}^p(\mathbf{M})^{\mathrm{T}} + \mathbf{Q}(t) \quad (2.6)$$

$$\mathbf{M} \equiv \frac{\partial}{\partial\mathbf{x}}\mathbf{m}(\mathbf{x}, t)\Big|_{\mathbf{x}=\mathbf{x}^p} \quad (2.7)$$

Stage 2: Update (probabilistic analysis)

$$\mathbf{x}^a = \mathbf{x}^p + \mathbf{K}\mathbf{d}^{op} \quad (2.12)$$

$$\mathbf{P}^a = (\mathbf{I} - \mathbf{K}\mathbf{H})\mathbf{P}^p \quad (2.13)$$

$$\mathbf{K} = \mathbf{P}^p\mathbf{H}^{\mathrm{T}}\left(\mathbf{H}\mathbf{P}^p\mathbf{H}^{\mathrm{T}} + \mathbf{R}\right)^{-1} \quad (2.14)$$

$$\text{subject to } \partial_{\mathbf{K}}\mathrm{tr}\mathbf{P}^a = 0$$

Fig. 1. A flow-chart representation of the EKF method (see Table 1 for definitions of the symbols).

Table 1
Nomenclature of EKF

$d\boldsymbol{\eta}$	Incremental stochastic forcing
$\mathbf{d}^{op}$	Difference between observation and model prediction in terms of $\mathbf{h}$
dt	Time step of integration
$\boldsymbol{\varepsilon}$	Observation's random error
E	Mathematical expectation
$\mathbf{h}$	Observation function
$\mathbf{H}$	Linearized transition matrix of observations
$\mathbf{I}$	Identity matrix
$\mathbf{K}$	Kalman gain matrix
$\mathbf{m}$	Deterministic forcing
$\mathbf{M}$	Linearized transition matrix of $\mathbf{m}$
$\mathbf{P}^a$	Model error covariance matrix after assimilation
$\mathbf{P}^p$	Predicted model error covariance matrix
$\mathbf{R}$	Observation error covariance matrix
t	Time
$\mathbf{Q}$	Error covariance matrix due to stochastic forcing
T	Transpose of a vector or matrix
tr	Trace of a matrix
$\mathbf{x}^a$, $\mathbf{x}^p$, $\mathbf{x}^t$	"assimilated", "predicted", and "true" state variables; $\Delta\mathbf{x}^p \equiv \mathbf{x}^p - \mathbf{x}^t$
$\mathbf{y}^o$	Observation function

2.2. An EKF extension for parameter optimization

Our EKF application to the optimal estimation of model parameters follows [13,12], where it was applied to the estimation of the ocean-atmosphere coupling parameters in an intermediate climate model of the tropical Pacific, and [15,16,18], where it was used for assimilating Lagrangian tracer observations to estimate the flow field. The parameter estimation is achieved by including both the state variables and the model parameters into an augmented state vector. Eq. (2.5) in Fig. 1 thus becomes

$$\frac{\mathrm{d}}{\mathrm{d}t}\mathbf{x}^p = \frac{\mathrm{d}}{\mathrm{d}t}\begin{pmatrix} \mathbf{x}_v^p \\ \boldsymbol{\mu}^p \end{pmatrix} = \begin{pmatrix} m_V(\mathbf{x}_v^p, t; \boldsymbol{\mu}^p) \\ 0 \end{pmatrix}, \tag{2.15}$$

where the subscript "v" represents state variables, the superscript "p" still denotes "prediction," as defined in Table 1, and the symbol $\boldsymbol{\mu}$ represents the vector of model parameters. The "true" state variables $\mathbf{x}_v^t$ are subject to both the system's deterministic and stochastic processes, as described in Eq. (2.1) in Fig. 1, while $\boldsymbol{\mu}$ is only subject to the stochastic processes, namely:

$$\mathrm{d}\boldsymbol{\mu}^t/\mathrm{d}t = d\boldsymbol{\eta}^\mu. \tag{2.16}$$

The magnitude of $d\boldsymbol{\eta}^\mu$ is determined as part of the overall system noise, $d\boldsymbol{\eta}$, as described in Section 4.1.

The counterpart of Eq. (2.6), which describes the time evolution of the error covariance matrix, now has four blocks:

$$\begin{aligned}
\frac{\mathrm{d}}{\mathrm{d}t}\mathbf{P}^p = \frac{\mathrm{d}}{\mathrm{d}t}\begin{pmatrix} \mathbf{P}_{vv}^p & \mathbf{P}_{\mu v\mu}^p \\ \mathbf{P}_{\mu v}^p & \mathbf{P}_{\mu\mu}^p \end{pmatrix} &= \begin{pmatrix} \mathbf{M}_{vv}^p & \mathbf{M}_{v\mu}^p \\ 0 & 0 \end{pmatrix}\begin{pmatrix} \mathbf{P}_{vv}^p & \mathbf{P}_{v\mu}^p \\ \mathbf{P}_{\mu v}^p & \mathbf{P}_{\mu\mu}^p \end{pmatrix} \\
&\quad + \left(\begin{pmatrix} \mathbf{M}_{vv}^p & \mathbf{M}_{v\mu}^p \\ 0 & 0 \end{pmatrix}\begin{pmatrix} \mathbf{P}_{vv}^p & \mathbf{P}_{v\mu}^p \\ \mathbf{P}_{\mu v}^p & \mathbf{P}_{\mu\mu}^p \end{pmatrix}\right)^T + \begin{pmatrix} \mathbf{Q}_{vv}^p & \mathbf{Q}_{v\mu}^p \\ \mathbf{Q}_{\mu v}^p & \mathbf{Q}_{\mu\mu}^p \end{pmatrix} \\
&= \begin{pmatrix} \mathbf{M}_{vv}^p \mathbf{P}_{vv}^p + \mathbf{M}_{v\mu}^p \mathbf{P}_{\mu v}^p & \mathbf{M}_{vv}^p \mathbf{P}_{v\mu}^p + \mathbf{M}_{v\mu}^p \mathbf{P}_{\mu\mu}^p \\ 0 & 0 \end{pmatrix} \\
&\quad + \begin{pmatrix} (\mathbf{M}_{vv}^p \mathbf{P}_{vv}^p + \mathbf{M}_{v\mu}^p \mathbf{P}_{\mu v}^p)^T & 0 \\ (\mathbf{M}_{vv}^p \mathbf{P}_{v\mu}^p + \mathbf{M}_{v\mu}^p \mathbf{P}_{\mu\mu}^p)^T & 0 \end{pmatrix} + \begin{pmatrix} \mathbf{Q}_{vv}^p & \mathbf{Q}_{v\mu}^p \\ \mathbf{Q}_{\mu v}^p & \mathbf{Q}_{\mu\mu}^p \end{pmatrix}.
\end{aligned} \tag{2.17}$$

The new error covariance matrix is defined as:

$$\begin{pmatrix} \mathbf{P}_{vv}^p & \mathbf{P}_{v\mu}^p \\ \mathbf{P}_{\mu v}^p & \mathbf{P}_{\mu\mu}^p \end{pmatrix} \equiv E\left[\begin{pmatrix} \mathbf{x}_v^p - \mathbf{x}_v^t \\ \boldsymbol{\mu}^p - \boldsymbol{\mu}^t \end{pmatrix} \begin{pmatrix} \mathbf{x}_v^p - \mathbf{x}_v^t \\ \boldsymbol{\mu}^p - \boldsymbol{\mu}^t \end{pmatrix}^{\mathrm{T}} \right]. \tag{2.18}$$

The original time evolution of the error-covariance matrix, as described by Eq. (2.6) in Fig. 1, is built into Eq. (2.17), as represented by the terms with the subscripts "vv". The extra errors associated with the model parameters originate from the system error-covariance in terms of $\mathbf{Q}_{\mu\mu}$. The expansion described by Eqs. (2.15)–(2.18) has an update stage similar to Eqs. (2.12)–(2.14), except that $\mathbf{H}$ now has a component contributed by $\boldsymbol{\mu}$.

3. MESA-1D code and flyer plate experiment

The Eulerian conservation equations for mass ρ, momentum u, internal energy e, and the equation of state (EOS) in our MESA-1D code [20] are summarized here using the total derivative $\mathrm{D}/\mathrm{D}t$:

$$\mathrm{D}\rho/\mathrm{D}t = -\rho u_x, \tag{3.1}$$

$$\rho \mathrm{D}u/\mathrm{D}t = -P_x, \tag{3.2}$$

$$\rho \mathrm{D}e/\mathrm{D}t = -P u_x, \tag{3.3}$$

$$P = p(\rho, e) + Q(\rho, \acute{\varepsilon}); \tag{3.4}$$

here the subscript x represents the partial derivatives with respect to the spatial coordinate x, P is the total pressure which is the sum of the EOS pressure p and the artificial viscosity Q, and is the total strain rate, which is equal to u_x. In this work a solid phase Mie-Grüeisen EOS is used with the form of

$$p = p_H + \Gamma[\rho_0 e - 0.5 p_H(v/(1+v))]. \tag{3.5}$$

The Hugoniot pressure p_H is given by

$$p_H = [\rho_0 c_0^2 v(1+v)]/[1 - v(s-1)]^2. \tag{3.6}$$

The artificial viscosity is defined as

$$Q = -C_L \rho c_0 \Delta x \acute{\varepsilon} + C_Q \rho \Delta x^2 \acute{\varepsilon}^2. \tag{3.7}$$

The parameters in Eqs. (3.5)–(3.7) are defined as follows: Γ is the Grüneisen parameter, ρ_0 is the initial density, v is the compression $\rho/\rho_0 - 1$, c_0 is the initial sound speed, Δx is the cell length, s is the shock velocity constant, and C_L and C_Q are artificial viscosity constants. Their standard values are given in Table 2.

Table 2
Model parameters

| Parameter	Description	Value
NC	Total number of grid cells	74
Δx	Grid size	0.0375 cm
$(NC)_{flyer}$	Number of grid cells in flyer plate	8
$(NC)_{target}$	Number of grid cells in target plate	48
$(NC)_{vacuum}$	Number of grid cells in vacuum regions	18 (9×2)
Δt	Maximum size of time step	0.01 μs
$u_{fp}(t=0)$	Initial velocity of flyer plate	0.0645 cm μs^{-1}
ρ_0, $\rho(t=0)$	Reference density in EOS, initial density	8.93 g cm^{-3}
Y	Yield stress	0.00103 Mbar
G	Shear modulus	0.50 Mbar
Γ	Gruneisen parameter	2.002
s	Shock velocity constant	1.489
c_0	Initial sound speed	0.394 cm μs^{-1}
C_L	Linear artificial viscosity constant	0.2
C_Q	Quadratic artificial viscosity constant	2.0
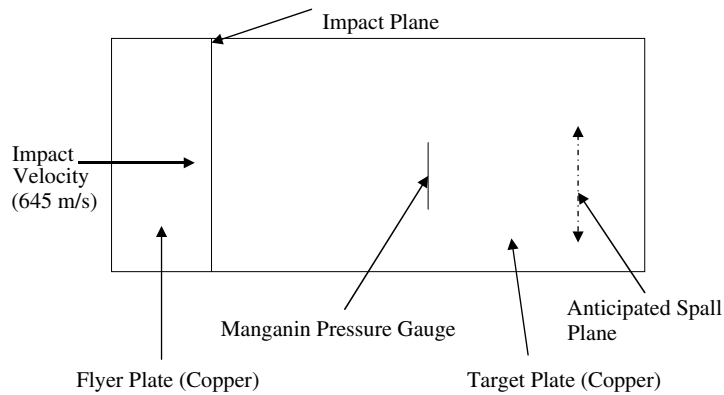
Fig. 2. A schematic diagram of the 1-D flyer plate experiment.
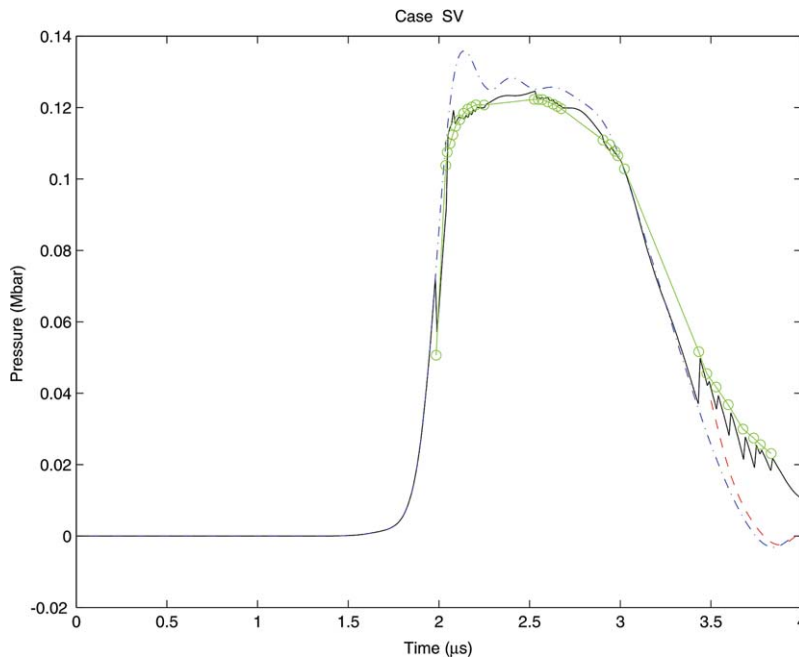

Fig. 3. Pressure evolution at the middle of the target plate with an observation error (w) of 0.1 kbar and a normalized model error (q) of 0.001. Green curve: fitted to the experimental data points marked by green circles; blue dash-dotted curve: pure prediction without EKF; black solid curve: assimilated evolution with EKF; red dashed curve: the evolution that the black curve would have undergone if no data were available after 3.4 μs.

A schematic diagram of the flyer-plate experiment is shown in Fig. 2. The flyer plate with a velocity of 0.0645 cm μs^{-1} (645 m s^{-1}) and a thickness of 0.3 cm impacts the stationary target plate that is six times thicker. This produces a shock that compresses the material to a Hugoniot pressure of about 20 Gpa at the impact plane. The shock waves travel into both plates with a speed of about 0.45 cm μs^{-1}, estimated from the Hugoniot data. These waves eventually reach the outer boundaries of the plates, where they reflect back into the plate interiors as rarefaction waves. The original numerical simulations [20,14] were performed using the model specifics and parameters summarized in Table 2. We have pressure data collected at the middle of the target plate by a Manganin pressure gauge [2] between 2.0 and 3.8 μs (cf. Fig. 3) after the impact. Therefore, most of the subsequent discussion regarding data assimilation with the EKF will be devoted to this time interval.

4. Results

4.1. EKF performance without parameter optimization

In this section, we briefly review the results in [20], where only the model state variables were optimized and the model parameters were based on Table 2. In this case, the variable vector **x** shown in Fig. 1 only includes the state variables $\mathbf{x}_V$, cf., Eq. (2.15), and we refer to this case as "SV." In the SV case, we assume the initial error-covariance matrix $\mathbf{P}^p$ to be zero. The error-covariance matrix $\mathbf{Q}^p$ is constructed from the system noise d**η** due to the discretization errors, evaluated against ultra-fine resolution runs [20]. Since the system noise is expressed as a random distribution function on grid cells, $\mathbf{Q}^p$ is thus simply a diagonal matrix with a uniform magnitude. The random distribution is bounded between the magnitudes of $\pm 10^{-3} \times \Phi$, where Φ represents the reference values of each state variable. Such magnitudes would result in a potential change of each state variable (cf., Eq. (2.1)) to be within $\pm 100\%$ of Φ after 1000 time-steps of integration. In the current case, Φ is set to be 10.0 g cm^{-3}, 10^{-1} cm μs^{-1}, and 10^{-3} Mbar cc g^{-1}, respectively, for density, velocity, and internal energy. Finally, the observation error of the pressure data measured by the Manganin pressure gauge is assumed to be 10^{-1} kbar (c.f., [20] for the sensitivity tests of observation errors).

Fig. 3 is reproduced from [20] and it shows the evolution of pressure with time at the middle of the target plate. It compares the results of pure model simulation and of data assimilation with the actual data. The pure prediction without any data assimilation (blue dash-dotted curve) exhibits a Gibbs phenomenon along its flat top portion, between 2.0 and 2.5 μs. The difference between this curve and the actual data (green curve) is obvious, especially during the release-wave interval, where the pressure starts to decrease with time. The result of assimilating the pressure data with the EKF (solid black curve) agrees rather well with the data points in green. The results show that, with the given observation and model errors, the data carry more weight in the optimization process than the model. Even though pressure was measured and assimilated only at the middle of the target plate, the effects of data assimilation are definitely not limited to this point and to this variable, as discussed in [20].

In Fig. 3, for the interval between 3.1 and 3.45 μs over which data are not available, the model run with EKF does not lead to a close match to the next available data; instead, it coincides with the pure prediction, as a result of the very similar state reached by the two runs at 3.1 μs. The sudden restoring feature at 3.45 μs in the black curve shows that the EKF has very high confidence in the data. The jagged variation in the black curve, from 3.5 to 4.0 μs, reflects the same situation: the prediction made by the EKF run between updates drifts away from the data until it is pulled back by the update process at each observation time. An additional simulation was made in which no more data points were used after the update at 3.4 μs (red dashed curve). This prediction for the rest of the simulation gradually merges with the blue dash-dotted curve that represents the pure prediction for the entire interval.

The problematic features discussed in the above paragraph are the results due to the problem that the pure prediction has a systematically sharper fall-off in pressure than the experimental data during the release-wave interval. This kind of model deficiency in simulating flyer-plate data has been well documented since1990s [22]. In this paper, as discussed in the introduction, we investigate the problem through the role of model parameters used in this class of models for shock wave studies.

4.2. Performance of EKF with parameter optimization

We refer to the case in which we attempt to optimize both state variables and model parameters as "SV + MP". The eight parameters chosen to form the vector **μ** of Eq. (2.15) are listed in Table 2, starting from the reference density in EOS (ρ_0) to the quadratic artificial viscosity constant (C_Q). For the sake of simplicity, the initial errors of **μ** are given by a uniform value of 1% of the original parameter values listed in Table 2, which, in turn, specify the initial variances of **μ** in the initial $\mathbf{P}^p_{\mu\mu}$ in Eq. (2.17). The system noise for **μ** is specified the same way as for $\mathbf{x}_V$, described in Section 4.1. The initial values of variances for **μ** represent our best estimate of the uncertainties of the model parameters before the shock interacts with the copper plates.

Fig. 4 shows the counterpart of Fig. 3 for the pressure evolution at the middle of the target plate in the case of SV + MP. There are two distinct differences between Figs. 3 and 4. The restoring zig-zag feature between
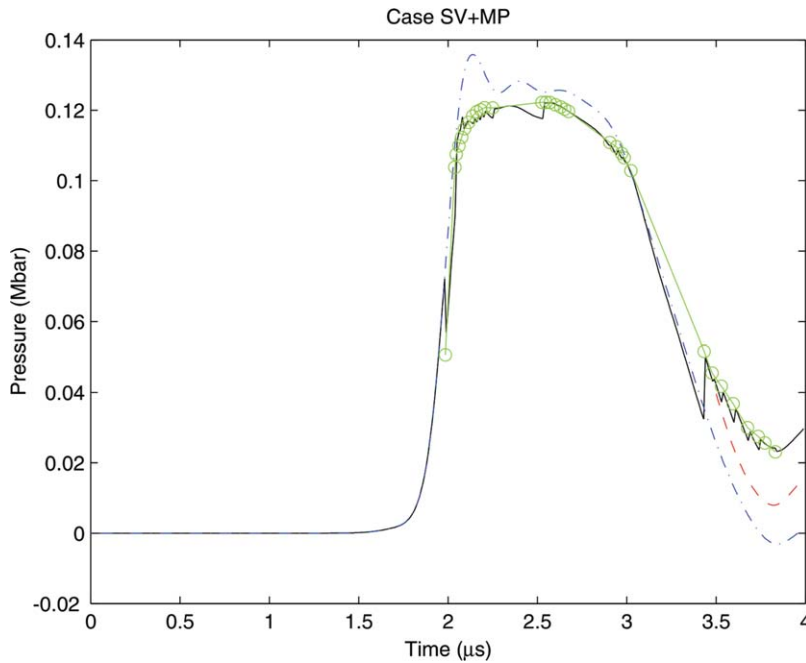
Fig. 4. Same as Fig. 3, except that the assimilation was done for both the model state variables and parameters (see Section 2.2).
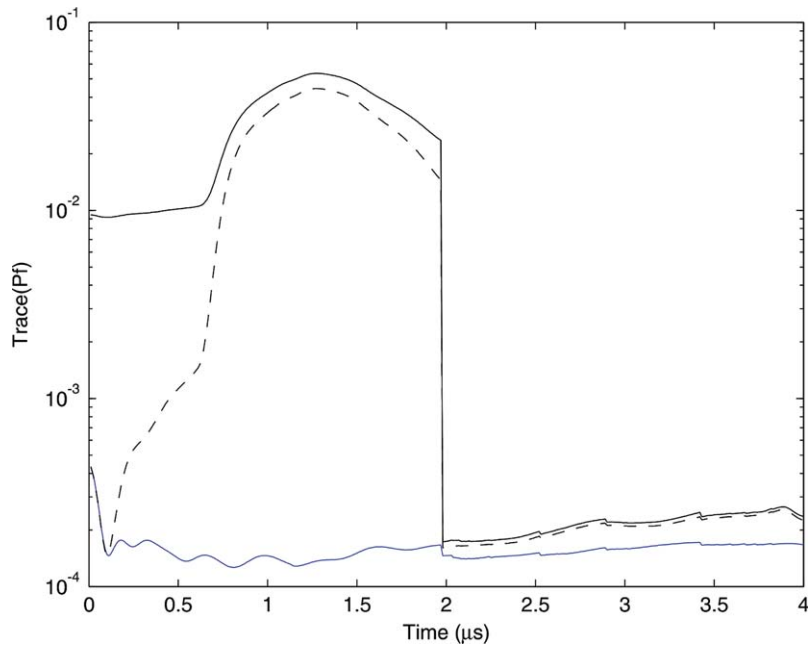

Fig. 5. The trace of $\mathbf{P}^p$ (the sum of the variances) as a function of time. Blue curve: assimilated evolution in the case of SV; black solid curve: assimilated evolution in the case of SV + MP; and black dashed curve: the trace of the state variables only in SV + MP.

3.5 and 3.8 μs, in the release interval, has a much smaller magnitude in Fig. 4, and the pure prediction after 3.4 μs (in red) agrees considerably better with the data (in green). Furthermore, the assimilated pressure shown in Fig. 4 is closer to the data values than in Fig. 3.
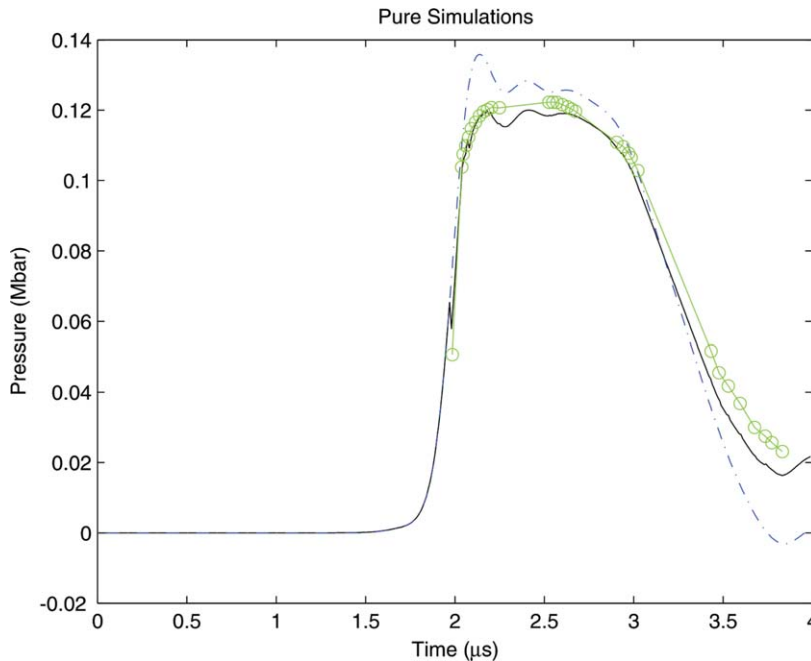
Fig. 6. Pressure as a function of time at the middle of the target plate from pure model simulations with the two different sets of parameters: blue dash-dotted curve: simulation with original time-constant parameters; and black solid curve: simulation with the optimized, time-varying model parameters. The former curve is identical to the blue dashed curve in Figs. 3 and 4. The green curve is fitted to the experimental data points marked by green circles.

The inclusion of the model parameters in the EKF formalism helps the model to better track the data during the energy release interval on two counts: the overall better agreement between the assimilated model state and the data prior to this interval, and the newly optimized model parameters. The former is directly due to the larger model errors associated with the introduction of the parameters' errors. Fig. 5 shows the trace of the error-covariance matrix $\mathbf{P}^p$ for both the SV and SV + MP cases, respectively, by the blue and black solid curves. The dashed black curve is the trace for only the state variables in SV + MP. Since the observational error is the same between the two cases, the Kalman gain is thus larger in SV + MP because of a larger model error, which leads to a larger weighting of the data in the assimilated fields. Recall that $\mathrm{tr}\mathbf{P}^p$ contains only the sum of the variances of the state variables in the SV case, while in the SV + MP case one has to add the sum of the model parameter variances.

Note in Fig. 5 that, prior to the first data point at 1.9 µs, the error of the model state variables in SV + MP is one to two orders of magnitude larger than that in SV by viewing the relative magnitudes between the solid and dashed black curves. The extra error introduced through the model parameters triggers a nonlinear amplification of the error in the state variables, as described by Eq. (2.17). Interestingly, the first data point alone brings the model error down to a level that is quite comparable to the SV case.

The second reason that we obtain a better assimilation and model evolution during the release period is due to the newly optimized model parameters. Fig. 6 shows the model prediction using the optimized, time-varying model parameters along with the one that uses the original parameters listed in Table 2. The use of the optimized model parameters makes the modeled pressure (the black curve) agree with the data curve (green) much better, both during the flat-top and the release periods. The model parameter values thus play a major role in modeling the laboratory shock-wave experiments.

We now examine the properties of the optimized model parameters. Three of the eight optimized parameters – the reference density ρ_0, sound speed c_0, and yield stress Y – are shown in Fig. 7 as a function of the "data time." The reference density is the most crucial parameter in describing the shock behavior through the equation of state (EOS), while the sound speed and yield stress affect the pressure evolution in the shock. In general, the evolution in time of all three model parameters resembles the simulated pressure shown in Fig. 3
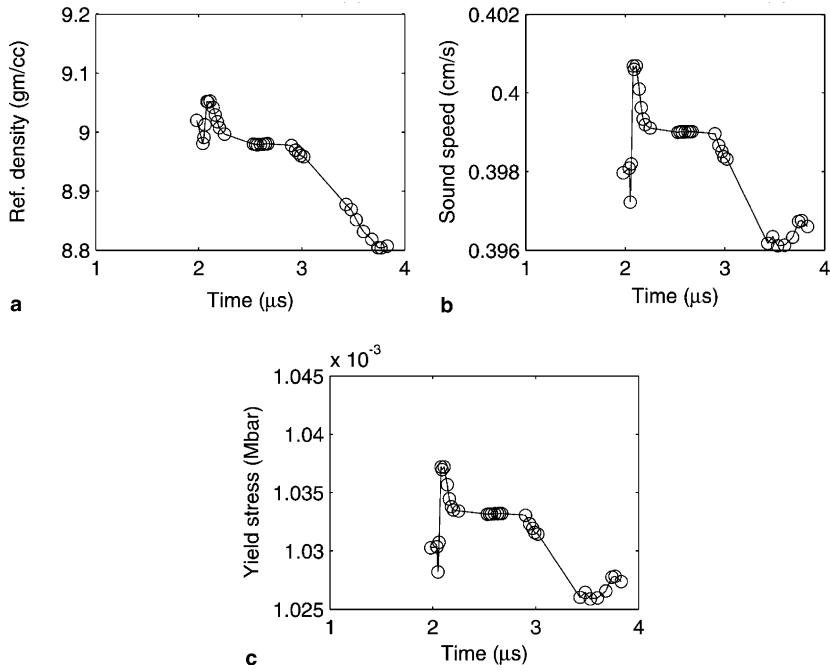
Fig. 7. The evolution of model parameters estimated using the data as a function of data time: (a) reference density used in equation of state; (b) sound speed used in Hugoniot pressure and artificial viscosity; and (c) yield stress used in the material constitutive model in the MESA code.
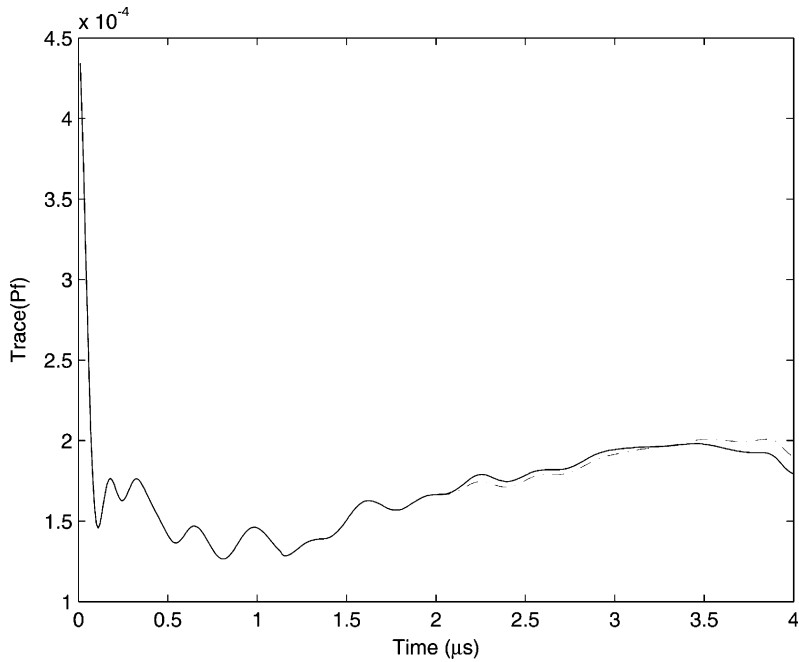

Fig. 8. The trace of $\mathbf{P}^p$ (the sum of the variances) as a function of time. Red dash-dotted curve: pure prediction with the original time-constant model parameters; black solid curve: pure prediction with the optimized model parameters. The red and black curves coincide with each other until the first data point at 1.9 μs.

or 4 (the blue dashed curve). The differences in the optimized parameters' values between the flat-top and energy-release periods have corresponding physical meanings. The lower density during the release period should correspond to a slower sound speed and a lower yield stress. The lower density arises from the fact that the target plate is experiencing a tensile force at the end of release period. Unphysical over-shooting of the modeled pressure explains the spiky features near 2.0 μs in all the parameters shown in Fig. 7. The evolution of the remaining five parameters being estimated resembles that shown in Fig. 7(b) and (c).

These results are important on two counts. First, a set of constant parameter values does not appear to physically correspond to both the flat-top and energy-release stages. Second, the variation of each model parameter ranges from 0.8% to 1.8% of its mean value, as partially indicated in Fig. 7. This is a range that is well within the accuracy tolerance of the measurement techniques under harsh conditions, and the sample variations in the case of copper density. Yet these optimized parameters greatly help the model performance, in particular during the energy-release period.

Fig. 8 shows the trace of the error-covariance matrix for the two model runs, respectively, with the time-constant and time-varying model parameters. Their corresponding simulations of the modeled pressure were shown in Fig. 6, which have a significant difference in performance. It is interesting to find that, in Fig. 8, the overall model error is also smaller in the release period. Even though the error reduction is only about 5%, it reflects our earlier point in the introduction that keeping model parameters constant is equivalent to letting the state variables absorb the uncertainties in the parameters. Since the model error represented by the error-covariance matrix is largely driven by the linearized transition matrix ($\mathbf{M}$), shown in Eq. (2.7), the optimized model parameters appear to help reduce the model's sensitivity through a linear sense.

5. Concluding remarks

This is the second part of our data assimilation studies for the modeling of shock wave in the laboratory experiments. Data assimilation [10] was introduced into continuum mechanics through its atmospheric and oceanographic applications [3,11]. We are not aware of any previous attempt to use data assimilation in high-speed impact studies or solid mechanics, except the effort presented here and our immediately previous work [20]. The only work we are aware of that applies data assimilation methods to laboratory experiments in continuum mechanics (aside from PIV, i.e., particle image velocimetry) was performed by [9].

A limited amount of experimental data was available for our studies from a flyer-plate laboratory experiment. To put this information for best use, we apply the extended Kalman filter (EKF) method (see Fig. 1) of data assimilation to a simple, but realistic 1-D hydrodynamic model, the MESA-1D code [4,20]. EKF solves the full nonlinear state evolution and its error-covariance matrix in time. EKF was designed to estimate the true state of, as well as reduce its uncertainties of, the modeled entity, provided that the errors of observations and model performance are known.

The results from the first part of our work [20] showed that, during the release period of the shock wave and in the absence of data assimilation, the model prediction has a systematically sharper fall-off in pressure than the experimental data. This systematic difference even makes the assimilated fields quickly tend toward the model's original evolution (i.e., the evolution without applying data assimilation). This results in the repetitively restoring features in the assimilated curve. It seems natural to attribute this discrepancy between model and experiment to a shortcoming the former. We are motivated to investigate the potential usefulness of using EKF to optimize not only the model's state variables but also its parameters. The present work was also based on the recognition that it may be inappropriate to use a set of time-constant model parameters for modeling the evolution of a shock wave, which separates two very different states of the medium through which it propagates.

Our modified assimilation technique adds the model parameters to the original state variable vector [10,13,12]. We further assume that variations in these parameters are only driven by the system's noise. The available pressure data at a single location are used to update both the state variables and model parameters. The updated model parameters (see Fig. 7) are considered optimized within the EKF framework, since they and the updated state variables collectively provide a minimized error-covariance matrix (see Figs. 5 and 6). When including these model parameters in the assimilation framework (Case SV + MP), the assimilated model fields are improved over the case where only the state variables were assimilated and the model parameters

were kept constant (Case SV). Furthermore, the pure simulation (i.e., without the application of data assimilation) with the optimized parameters performs much better than the counterpart using the original parameters.

Model parameters have been so far treated as constant in time in simulation throughout continuum mechanics and even in shock-wave research. The current study indicates that keeping model parameters constant in time can be the primary culprit for certain systematic discrepancies between modeled results and experimental data. Since we do not have a priori knowledge about the potential variation of a model parameter, the methodology proposed here should be useful in ascertaining such a variation for certain physical systems and their associated overall uncertainties. Our methodology is based upon the recognition of two important facts: (1) the model parameters are subject to uncertainties, just like the model's state variables; and (2) when the system undergoes major changes in its physical regime, a time-constant parameter may not serve the purpose. The latter is especially true for the current study of shock dynamics, but may be relevant to many other situations in continuum mechanics, like fracture problems, flow in porous media, or the propagation of fronts (i.e., contact discontinuities) in the atmosphere and oceans.

This work can be extended into two directions. First, one can make more extensive use of data from different experimental designs and material samples within the areas of shock compression and high-pressure science and technology. With our proposed EKF method, one can track the evolution in time of model parameters and of their uncertainties. One can even go further to infer the physical, deterministic connections between model's state and its parameters. Second, the current implementation of EKF is computationally expensive for multi-dimensional problems due to the need to calculate time-dependent error-covariance matrices. Different approaches exits to overcome this obstacle and to minimize the computational cost. They include the ensemble approach [1,5,6], the wavelet technique [19], and reduced-rank filters [11,7,8].

Acknowledgments

References

[1] J.L. Anderson, An ensemble adjustment filter for data assimilation, Mon. Weather Rev. 129 (2001) 2884–2903.

[2] K.M. Baker, M. Shahinpoor, L.C. Chhabildas, in: J.R. Asay, M. Shahinpoor (Eds.), High-Pressure Shock Compression of solids, Springer, 1993, p. 43.

[3] L. Bengtsson, M. Ghil, E. Källén (Eds.), Dynamic Meteorology: Data Assimilation Methods, Springer, New York/Heidelberg/Berlin, 1981, p. 330.

[4] D.J. Cagliostro, D.A. Mandell, L.A. Schwalbe, T.F. Adams, E.J. Chapyak, MESA 3-D calculations of armor penetration by projectiles with combined obliquity and yaw, Int. J. Impact Eng. 10 (1990).

[5] C.L. Keppenne, Data assimilation into a primitive-equation model with a parallel ensemble Kalman filter, Mon. Weather Rev. 128 (2000) 1971–1981.

[6] C.L. Keppenne, M.M. Rienecker, Initial testing of a massively parallel ensemble Kalman filter with the Poseidon isopycnal ocean general circulation model, Mon. Weather Rev. 130 (2002) 2951–2965.

[7] S.E. Cohn, R. Todling, Approximate data assimilation schemes for stable and unstable dynamics, J. Meteorol. Soc. Japan 74 (1996) 63–75.

[8] I. Fukumori, T. Lee, B. Cheng, D. Menemenlis, The origin, pathway, and destination of Niño-3 water estimated by a simulated passive tracer and its adjoint, J. Phys. Oceanogr. 34 (2004) 582–604.

[9] M.J. Galmiche, Sommeria, E. Thivolle-Cazat, J. Verron, Using data assimilation in numerical simulation of experimental geophysical flows, C. R. Acad. Sci. 331 (2003) 843–848.

[10] A. Gelb (Ed.), Applied Optimal Estimation, The MIT Press, 1974, p. 347.

[11] M. Ghil, P. Malanotte-Rizzoli, Data assimilation in meteorology and oceanography, Adv. Geophys. 33 (1991) 141–226.

[12] M. Ghil, Advances in sequential estimation for atmospheric and oceanic flows, J. Meteor. Soc. Japan 75 (1997) 289–304.

[13] Z. Hao, M. Ghil, Sequential parameter estimation for a coupled ocean-atmosphere model, in: 2nd International Symposium on Assimilation of Observations in Meteorology and Oceanography, World Meteorological Organization, Tokyo, Japan, 13–17, vol. 1, 1995, pp. 181–186.

[14] R.J. Henninger, P.J. Maudlin, M.L. Rightley, Accuracy of differential sensitivity for one-dimensional shock problems, in: APS Shock Compression of Condensed Matter Conference, Amherst, MA, 1997.

[15] K. Ide, M. Ghil, Extended Kalman filtering for vortex systems. Part I: Methodology and point vortices, Dyn. Atmos. Oceans 27 (1997) 301–332.

[16] K. Ide, M. Ghil, Extended Kalman filtering for vortex systems. Part II: Rankine vortices and observing-system design, Dyn. Atmos. Oceans 27 (1997) 333–350.

[17] K. Ide, P. Courtier, M. Ghil, A. Lorenc, Unified notation for data assimilation: Operational, sequential and variational, J. Meteor. Soc. Japan 75 (1997) 181–189.

[18] K. Ide, L. Kuznetsov, C.K.R.T. Jones, Lagrangian data assimilation for point vortex systems, J. Turbul. 3 (2002) 53–59.

[19] L. Jameson, T. Waseda, Error estimation using wavelet analysis for data assimilation: EEWADAi, J. Atmos., Oceanic Technol. 17 (2000) 1235–1246.

[20] J. Kao, D. Flicker, R. Henninger, S. Frey, M. Ghil, K. Ide, Data assimilation with an extended Kalman filter for an impact-produced shock-wave study, J. Comp. Phys. 196 (2004) 705–723.

[21] L. Ljung, System Identification: The Theory for the User, Prentice Hall, 1987, 519pp.

[22] P.J. Maudlin, R.F. Davidson, R.J. Henninger, Implementation and assessment of the mechanical-threshold-stress model using EPIC2 and PINON computer codes, LA-11895-MS, Los Alamos National Laboratory Report, 1990.

[23] R.N. Miller, M. Ghil, F. Gauthiez, Advanced data assimilation in strongly nonlinear dynamical systems, J. Atmos. Sci. 51 (1994) 1037–1056.

[24] I.M. Navon, Practical and theoretical aspects of adjoint parameter estimation and identifiability in meteorology and oceanography, Dyn. Atmos. Oceans 27 (1998) 55–79.

[25] J.A. Zukas (Ed.), High Velocity Impact Dynamics, Wiley, 1990, p. 935.